Journal of the European Ceramic Society **18** (1998) 1545–1558

PII: S0955-2219(98)00074-0
0955-2219/98/$—see front matter

The Combination of Equilibrium and Dynamic Methods for the Detailed Structural Characterisation of Ceramic Membranes

A. Ch. Mitropoulos, K. Beltsios, Th. A. Steriotis,* F. K. Katsaros, P. Makri and N. K. Kanellopoulos

Institute of Physical Chemistry, National Center for Scientific Research 'Demokritos', 15310 Ag. Paraskevi Attikis, Greece

(Received 14 November 1997; accepted 16 February 1998)

Abstract

The combination of equilibrium and dynamic techniques provides powerful tools for the characterisation of the porous structure of ceramic membranes. We present the type of information obtainable by the permeability, adsorption and small angle scattering (SAS) methods and important combinations of them. Subsequently, we apply selected combinations of the above methods to three characteristic ceramic membrane materials: (a) a mesoporous alumina produced by symmetric compaction, (b) a Vycor®-type mesoporous silica, and (c) an asymmetric carbon membrane with a microporous gas-separating layer. Important conclusions are drawn regarding the pore and internal surface morphology of the studied membranes. © *1998 Elsevier Science Limited. All rights reserved*

Nomenclature

A_o	surface area at $p/p_0 = 0$ (cm^2/cm^3 membrane)
A_x	surface area at $p/p_o = x$ (cm^2/cm^3 membrane)
A_R	relative surface area
B_0	geometrical term (cm^2)
c	molecular concentration inside the pore space (moles cm^{-3})
C_N	coordination number
d	characteristic dimension of the scatterers (Å)
D	diffusion coefficient ($cm^2\,sec^{-1}$)
D_{cyl}	theoretical diffusion coefficient for cylindrical pores ($cm^2\,s^{-1}$)
D_{exp}	experimental diffusion coefficient ($cm^2\,s^{-1}$)
D_f	fractal dimension
D_g	gas diffusion coefficient ($cm^2\,s^{-1}$)
D_K	Knudsen diffusion coefficient ($cm^2\,s^{-1}$)
$\langle D \rangle$	mean density of CO_2 inside the pore (molecules nm^{-3})
E	activation energy (Kcal $mole^{-1}$)
h	half length of cylinder/thickness of disk (Å)
$I(Q)$	scattering intensity
I_o	Guinier's constant
J_D	diffusive flux, driven by the chemical potential, $\partial\mu/\partial x$ (moles $cm^{-2}\,s^{-1}$)
J_V	Viscous flux, driven by the pressure gradient, $\partial p/\partial x$ (moles $cm^{-2}\,s^{-1}$)
k	Boltzman constant
ℓ_c	correlation length (Å)
n_T	connectivity
P	permeability ($cm^2\,s^{-1}$)
p/p_0	relative pressure
P_R	relative permeability
Q	scattering vector ($Å^{-1}$)
$\tilde{Q}_x$	Porod invariant at $p/p_0 = x$
$\tilde{Q}_0$	Porod invariant at $p/p_0 = 0$
R	gas constant
r_c	radius of cylinder (Å)
r_d	radius of disk (Å)
r_e	equivalent radius (Å)
R_G	radius of gyration (Å)
r_k	Kelvin radius (Å)
r_m	mean radius (Å)
r_p	pore radius (Å)
S	specific surface area ($m^2\,g^{-1}$)
T	temperature (K)
t	film thickness (Å)
T_c	critical temperature (K)
V	scattering volume (cm^3)
V_L	molar volume ($cm^3\,mol^{-1}$)
V_s	volume sorbed (cm^3 STP g^{-1})

*To whom correspondence should be addressed.

V_t	total volume sorbed (cm^3 STP g^{-1})
w	pore width (Å)

Greek symbols

γ	surface tension (dyn cm^{-1})
$\gamma(r)$	correlation function
η	viscosity coefficient (poise)
ϑ	half scattering angle (degreee)
κ_g	structure factor obtainable from plain permeability measurements
λ	wavelength (Å)
$\bar{\lambda}$	mean free path (Å)
ρ	scattering length/electron density ($Å^{-2}$)
φ_p	volume fraction of the pores (porosity)
φ_x	volume fraction of the amount adsorbed at $p/p_0 = x$

1 Introduction

Membrane technology is of great industrial interest, as in many cases it can replace traditional, pollution-prone and energy consuming separation processes. A thorough assessment of the structural features of the pore network is a quite important part of the characterisation of a membrane system and a number of equilibrium and dynamic experimental techniques is used for that purpose.

In this work, we briefly survey three independent methods of pore structure characterisation (permeability, adsorption, small-angle scattering (SAS) of X-rays and neutrons) and two significant combinations of them (permeability in conjunction with adsorption and adsorption in conjunction with SAS), with special emphasis on the type of information obtainable in each case. Subsequently, we demonstrate the application of the full range of the above methods to a mesoporous alumina membrane. In the case of a mesoporous Vycor®-silica membrane, we use adsorption in conjunction with SAS for the study of the special feature of a fractal pore surface. Finally, we combine structural models with those of the above methods appropriate for microporous materials for the study of a carbon membrane with a microporous gas-separating layer.

2 Dynamic and Equilibrium Methods and Selected Combinations for the Study of Ceramic Membranes

2.1 Adsorption

Adsorption is the most popular pore analysis equilibrium technique. The adsorption isotherm of gases or vapours on a solid, provides information about the pore volume and the pore structure of the solid.

Adsorption isotherms are classified by Brunauer *et al.* [1] in five types according to the pore size of the solid and the adsorbent-adsorbate interaction, with the shape of the isotherm being indicative of the presence of certain types of pores (micropores, i.e. pores with width, w, less than 20 Å, mesopores, i.e. 20 Å $< w <$ 500 Å and macropores with $w >$ 500 Å).

Analysing the data with different adsorption models (BET, Langmuir) specific surface area and micropore volume can be obtained, while surface energetic heterogeneity can be determined by the isosteric heat of adsorption.

The pore size distribution (psd) of mesoporous solids can be derived through well-established isotherm analysis methods,[2] based on the Kelvin equation:

$$\ln\left(\frac{p}{p_0}\right) = -\frac{2V_L\gamma}{RTr_k} \tag{1}$$

where p/p_0 is relative pressure, V_L is molar volume, R is gas constant, T is absolute temperature and r_k is the Kelvin radius.

Clearly the above analysis can be only applied to pores accessible to the penetrating gas (open pores), while inaccessible (closed) pores can only be detected with the aid of other methods such as SAS (see below). Further, Kelvin equation is not applicable to microporous materials, due to the small size of pores (few molecular diameters) and the overlapping potential fields of neighbouring walls. In the latter case the processing of adsorption data using the potential theory[3] is possible and can lead to psd estimates of semi-quantitative validity.

2.2 Permeability

Permeability is a dynamic characterisation technique and relies on the study of fluid flow properties of porous media, which are extremely sensitive functions of the pore size distribution (psd) and of additional pore structural characteristics, such as the pore shape and connectivity. The method is applicable both to microporous and mesoporous membranes.

Permeability measurements of a weakly adsorbed gas (such as helium) through the membrane, lead to the direct evaluation of gas diffusion coefficient, D_g. As the pressure gradient across the porous membrane increases, the flow regime changes from Knudsen to viscous (Poisseuille) flow, while surface flow occurs when the flowing gas (or vapour) is adsorbed on the walls of the porous

structure. On Knudsen flow, which occurs when the pore radius, r, is sufficiently smaller than the mean free path, $\bar{\lambda}$, of the flowing molecules ($r < 0{\cdot}05\bar{\lambda}$), D_K (Knudsen diffusion coefficient) is independent of the pressure gradient. Thus, one can easily detect the existence of defects in the porous structure by examining whether D_g is constant over a range of pressure gradients or not.

Since the actual pore networks have rather complex geometry, Barrer and co-workers,[4,5] have introduced a structure factor κ_g defined by the following equation:

$$\kappa_g = D_{\text{exp}}/D_{\text{cyl}} \tag{2}$$

The structure factor κ_g provides a connection between D_{cyl}, the theoretical (statistical mechanical) diffusion coefficient for cylindrical pores and D_{exp}, the experimentally measured diffusion coefficient. This factor can be estimated from permeability measurements and its magnitude, in combination with other available structural information (such as porosity and inhomogeneity details) can lead to some general conclusions about the pore network geometry.[5–7] As a detailed evaluation of the pore characteristics from dynamic data alone is very difficult, the flow characterisation methods are rarely used as prime tools in pore structure studies.

Additionally, the dependence of D_K on temperature, is of major importance, revealing whether diffusion is thermally activated ($D \propto e^{-E/RT}$) or not ($D \propto T^{1/2}$). Activated diffusion takes place when the molecules must surmount an energy barrier, usually produced by constrictions at the pore mouths. In this case the activation energy can be calculated.

On the other hand, differential permeability measurements of adsorbable gases or vapours through mesoporous media, performed at relative pressures (p/p_0) ranging from 0 to 1, exhibit a maximum at a certain p/p_0. This fact is attributed to the occurrence of capillary condensation in the mesopores according to Kelvin equation. Using appropriate models to simulate the process, structural characteristics of the porous media can be deduced. Recent investigations on microporous membranes[8] have shown that a peak analogous to the mesopore case appears, in the differential permeability versus mean pressure curve, even at temperatures above the critical. However, correlation of such peaks and pore structure is, at present, rather qualitative, due to the limited knowledge regarding the static and dynamic behaviour of the fluid in micropores.[9]

We may note that open pores can be either conductive or blind (dead-end). Both open pore types contribute to adsorption, while permeation occurs through conducting pores only.

2.3 Small angle scattering

In the small angle scattering (SAS) practice, either with neutrons (SANS) or X-rays (SAXS), most of the structural information is contained in the interval:

$$\pi/6 \leq Q \cdot d \leq 2\pi$$

where d is a characteristic dimension of the structure, and $Q = \frac{4\pi \sin \vartheta}{\lambda}$, where 2ϑ is the scattering angle and λ is the wavelength. The SAS techniques can detect structural entities (pores or solid domains) larger than 10 Å, with best results obtained for entities larger than 20 Å.

For an isotropic scatterer, the spherically averaged intensities $I(Q)$ may be represented by the integral:[10]

$$I(Q) = 4\pi\rho^2\varphi_p(1-\varphi_p)V\int_0^\infty r^2\gamma(r)\frac{\sin Qr}{Qr}\,\mathrm{d}r \tag{3}$$

where V is the scattering volume, ρ is the electron density or the scattering length density (sld), $\gamma(r)$ is the correlation function at point r, φ_P is the porosity of the sample and Q is the scattering vector defined above.

The above equation reduces to two well-known simpler forms, in two special cases:[11]

(a) At large Q values (when: $Q \cdot d_{\text{min}} \geq \pi$, where d_{min} is the smallest characteristic dimension affecting scattering), eqn (3) reduces to 'Porod's Law':

$$I(Q) = \frac{2\pi\rho^2 A}{Q^4} \tag{4}$$

from which the surface area, A, can be calculated. When the pore surface is fractal the fractal dimension, D_{f}, may be calculated by considering:

$$\log I(Q) \propto D_f - 6 \tag{5}$$

according to Bale and Schmidt[12]

(b) At low Q values (when $Q \cdot d_{\text{max}} \cdot \leqslant \pi/6$), we obtain the 'Guinier approximation':

$$I(Q) = I_0 \exp\left(-\frac{Q^2 R_G^2}{3}\right) \quad (6a)$$

where I_0 is a constant and R_G is the radius of gyration. Equation (6a) holds for scatterers with a spherical symmetry (i.e. spherical entities), while the following eqns (6b) and (6c) are obtained for scatterers having, respectively, a cylindrical and disc-like shape:[13]

$$I(Q) = I_0 \pi / 2Qh \exp(-Q^2 r_c^2/4) \quad (6b)$$

where r_c is the radius of the cylinder and $2h$ its length.

$$I(Q) = I_0 2/Q^2 r_d \exp(-Q^2 h^2/3) \quad (6c)$$

where r_d is the radius of the disc and h its thickness.

Equations (6a)—(6c) give rise to a technique known as 'modified Guinier analysis' which permits the determination of both the shape and the dimensions of the scattering entities. The shape and size of the scatterers is determined through examination of the fitting of the scattering data to appropriate plots corresponding to the three equations [for example, eqn (6b) implies that $\ln[QI(Q)]$ versus Q^2 is the appropriate test-plot for cylindrical scatterers]. When the actual shape of the scatterers is spherical (or some other shape of low asymmetry, e.g. a cube), the plots for cylindrical and disc-type shape will often yield negative values (having no physical meaning) for one of the dimensions of the scattering entities.

Additionally, by using specially developed software,[14] the scatterers size range of interest may be divided to a desired number of intervals, with a spline distribution assigned to each interval, allowing a different weight as a free variable. The size distribution of the scatterers can be determined by least square fitting to the experimental scattering curve and matrix inversion.

Finally, we may note that SAS may detect both open (either conducting or not) and closed pores.

2.4 Permeability in conjunction with adsorption (relative permeability)

Permeability in conjunction with adsorption or relative permeability (P_R), is a technique which combines dynamic data (permeability) with static measurements (adsorption) in a systematic manner and can become a source of detailed porous structure information.[5]

The relative permeability technique is based on the monitoring of the permeability, P, of a weakly adsorbed gas, such as helium, through a porous membrane partially blocked by a second dense adsorbate phase. The plot of P, normalised to the permeability at zero content, versus the volume adsorbed (normalised with respect to maximum content) is the P_R curve. Upon adsorption, a layer of adsorbate is building up on the walls of the pores and, when condensation occurs additionally, all the pores with radii smaller than a critical value are blocked. Thus, the P_R curve reveals the influence of different classes of pores on the flow properties of the medium.

The P_R curve crosses the normalised adsorbed volume axis at a certain value lower than unity. At this point (percolation threshold) the last open continuous path of the membrane system is blocked and no flow through the system occurs. The initial slope of the curve and the percolation threshold depend strongly on the pore connectivity, n_T. By application of the Effective Medium Theory[15] (EMT) to a stochastic network, an analytical expression relating P_R of a partially blocked mesoporous solid with n_T and the moments of the PSD, can be developed.[16] Using the best fitting simulation curve the actual pore connectivity can be estimated.

In the case of microporous materials, relative permeability technique can also be used as an easy and quick test for defect-free membranes as pointed out by Steriotis *et al.*[7]

2.5 Adsorption in conjunction with SAS

For a two-phase (e.g. solid-pores) system, with corresponding electron densities (or scattering length densities, sld) equal to ρ_1 and ρ_2, the scattering intensity $I(Q)$ is proportional to $(\rho_1 - \rho_2)^2$. Hence, when ρ_1 is equal to ρ_2 contrast matching is attained. As a result, small-angle scattering (SAS) performed in conjunction with adsorption can provide useful data, performing standard SAS analysis (Surface area, psd, fractality, R_G) for different classes of pores. In the case of SANS, an appropriate mixture of molecules of different hydrogen isotopes (e.g. H_2O/D_2O or C_6H_6/C_6D_6) may be used as a contrast matching adsorbate for a wide range of materials, whereas a case-specific substance having an electron density similar to that of the solid is required for SAXS. By determining a number of scattering curves at various p/p_0, the two equilibrium methods (Adsorption and SAS) are applied simultaneously. For mesoporous solids, a reconstruction of the adsorption isotherm can be attained.[17]

Since the specific area can be estimated from SAS measurements at various p/p_0, a relative area, A_R, plot (surface normalised to the total surface area of the outgassed sample versus p/p_0) can be

drawn. Taking advantage of appropriate models[18–20] a theoretical A_R curve can be estimated and may be used for the deduction of the co-ordination number (C_N) of the structural entities of the porous solid.

Finally, this technique can be used to detect changes in the porous structure or in some physicochemical properties of the surface, during adsorption. A typical example is the monitoring the defractalisation process of a fractal surface, as the equilibrium pressure increases.

2.6 Characterisation of microporous membranes

In the case of microporous materials, the adsorption results can not be quantified satisfactorily and, in addition, the SAS techniques can not detect structural entities smaller than 10 Å. As a result the adsorption in conjunction with SAS method, is not suitable for the quantitative study of microporous ceramic membranes. Still, SAS alone will often allow for a reliable probing of a microporous membrane. This is possible in the following two general cases: (a) the micropore diameter is larger than 10 Å and, preferably, than 15 Å, (b) the solid domains of the microporous material are larger than 10 or 15 Å. In the second case, the pore network information will be obtained indirectly, as SAS will provide direct information about the solid network, i.e. the structure complementary to the pore network. Such an approach may eventually reveal information about pores smaller than 10 Å, provided that the solid domains are larger than the corresponding pores. In particular, for materials with low or medium porosities (i.e. up to 0·5), the main features of the solid domains are often larger by a factor of 2 or 3 than the corresponding pores.

Further examination tools include the wide angle X-ray technique, which will yield Bragg peaks for structural entities (pores or solid domains) smaller than 10 Å. Actually, this is done routinely in the special case of microporous zeolites, for which the sizes of pores show a very narrow distribution as the pores are part of the crystalline structure of the material.

For materials bearing micropores that are not part of a crystal structure the information obtained from a plain SAS and/or a wide angle X-ray technique may be combined with the results of nitrogen adsorption (porosimetry) and gas permeability measurements and tested against various models for the membrane microstructure. The degree of success of such an approach will depend to some extent on the geometrical characteristics of the microporous material under examination.

For pore sizes smaller than approximately 10 Å, the membrane pore size may also be assessed with the help of a series of organic probe molecules. However, it should be noted that the permeability of vapours of appropriate substances will require a continuous path of pores having a minimum dimension larger than the diameter of the probe molecules. A complication that often arises in practice is that the microporous structure contains paths that allow certain probe molecules to enter the one side of the membrane but not to exit from the other. Subsequent degassing may then become rather cumbersome and in situ burning of the probe molecules is, in general, not possible as the membranes are usually sealed and held in place with the help of an organic resin. Recent studies of microporous membranes indicate that the differential permeability measurements of slightly supercritical carbon dioxide (temperature of experiment: 35°C, T_c for bulk carbon dioxide: 31°C) for pressures up to 60 bar, may eventually lead to a technique appropriate for the assessment of the pore structure of microporous membranes. Experimentation with a microporous carbon membrane and nanoporous Vycor®membranes having their surface modified by various types of continuous or near continuous microporous layers, show that the permeability of carbon dioxide as a function of pressure passes through a maximum.[8] The value of the maximum is probably a function of the pore size and the physical chemical nature of the pore walls as well, but for materials with similar physical chemical characteristics the maximum appears to shift to smaller values with smaller pore sizes.[21] Nevertheless, a systematic use of this test may have to await for the development of a quantitative interpretation of the observed permeability maximum based on Non-Equilibrium Molecular Dynamics (NEMD) modelling.

3 Experimental Procedure

The following materials were used in the present study:

1. An alumina porous pellet, with 43% porosity. The pellet was prepared by symmetrical compaction of alumina powder in eleven sections. Degussa aluminium oxide of type-C, with a mean particle radius $\approx$100 Å, was used for this purpose. During the compaction process, specific care was taken to avoid non-homogeneity effects. This was achieved by applying an appropriate level of compression to each segment of the pellet.
2. A Vycor®7930 type of porous silica in powder form and particle form (linear dimension $\approx$1 mm). According to the manufacturer

(Corning) the sample has a porosity of ≈28% and pores of ≈40 Å diameter.

3. An asymmetric gas-separating carbon membrane obtained through carbonisation of a novolac and a resole resin precursor and subsequent activation in a controlled (CO_2) environment.[8] The asymmetric membrane is of the composite type, with a microporous carbon skin and a macroporous carbon substrate. Several grades of the composite membrane are produced through a variation of the processing conditions (reaction times and temperatures). In addition, a membrane replica of the microporous skin is formed and activated under the same conditions as the original composite membrane. The skin replica serves as a reference material allowing the separate probing (through SAS and nitrogen adsorption) of the microporous component of the composite membrane and it is made of the same material as the original skin. In all cases the pore diameter of the microporous material appears to be in the 12–15 Å range, while the microporosity is 30% or more (larger for longer activation times).

The conditions for the application of the various characterisation methods are the following:

3.1 Adsorption

N_2 measurements at 77, were performed on alumina and carbon membranes with Quantachrome Autosorb-1, with Krypton upgrade, volumetric porosimeter. Measurements of H_2O, for Vycor and alumina, and CH_2Br_2, for Vycor®, at 22°C were obtained gravimetrically. Isothermal conditions were achieved via an oil bath, ensuring an absolute error of ±0·05°C.

3.2 Permeability

Absolute permeability measurements of He through alumina and carbon membranes were carried out under vacuum on a glass relative permeability apparatus.[7] Differential CO_2 permeability through carbon and Vycor® membranes were carried out under high pressure (0–70 bar) in a metal permeability–selectivity apparatus.[22]

3.3 Small angle scattering

SANS experiments on alumina and Vycor® were conducted at Hahn-Meitner-Institut. The incoming neutrons were monochromized by a mechanical speed selector and collimated on a variable length from 1 to 16 m. A two-dimensional ^{3}He-Detector with 32×32 elements of 10×10 mm^2 was used. The SANS data were recorded in a Q range between 0·00335 and 0·24 Å^{-1} and subsequently corrected for a detector efficiency, absolute intensity calibration and background.

3.4 Permeability in conjunction with adsorption (relative permeability)

Helium relative permeability experiments, through the alumina membrane, were carried out using the simplified technique proposed by Steriotis *et al.*[16] After equilibrating the porous membrane with the appropriate relative pressure of water vapour at 273 K, the high and low pressure sections were evacuated. Upon evacuation, helium was admitted in the high pressure section and allowed to penetrate in the low pressure section. The desorption rate was reasonably low so the linearity of the permeation curve remained unaffected by the desorption process for a period of a few minutes that was required to complete the experiment.

3.5 Adsorption in conjunction with SAS

Adsorption measurements in conjunction with SANS were also carried out at Hahn-Meitner-Institut. Mixtures of H_2O/D_2O were used as the adsorbates for the alumina and Vycor®. An appropriately modified Hellma cuvette of the type QS-0·100 was used as the sample cell and isothermal conditions (22·0 ± 0·1°C) were employed.

Small angle X-ray scattering experiments were carried out in a Q range from 0·005 to 0·15 Å^{-1}. The X-rays were produced using a copper anode X-ray tube and $\lambda = 1{\cdot}54$ Å was the selected wavelength. Monochromatization and collimation of the beam were also held. The main feature of the apparatus was a two-dimensional X-ray imaging system connected with a minicomputer frame. Contrast matching was attained by using dibromomethane as the adsorbate, while a special cell described elsewhere[17] was designed.

4 Results and Discussion

4.1 Alumina mesoporous membrane

Membranes made of compacted alumina particles are mesoporous materials with uniform and well-defined pore structure. Hence they are quite appropriate for structural studies by SANS, adsorption and relative permeability.

By performing standard BET analysis on the adsorption isotherms (N_2, H_2O) specific surface area, S (m^2 g^{-1}) or A (m^2 m^{-3} of the membrane), of the alumina membrane was calculated. Additionally, total pore volume (Gurvitsch volume) and porosity, φ_p, as well as the pore size distribution were estimated. From the values of φ_p and A the equivalent cylindrical radius, $r_e (r_e = 2\varphi_p/A)$ was found to be $r_e = 42{\cdot}06$ Å. Table 1 summarises the

Table 1. Structural and dynamic properties of the compacted Al_2O_3 membrane

	Adsorption			*SANS*	
	$S_{N_2}^{BET}$	$S_{H_2O}^{BET}$	*Macroscopic measurements*	$S_{p/p_0=0}^{SANS}$	
$S(m^2\,g^{-1})$	96·65	95·93	96·65	104·75	
TPV ($cm^3\,g^{-1}$)	0·25	0·23	0·23		
φ_p	0·45	0·43	0·43		
$A\times10^8$ (m^2/m^3)	1·73	1·79	1·81		
		$r_e = 2\varphi_p/A$		r_m[b]	ℓ_C
r(Å)	52·46	47·95	47·60[a]	41·07	46·57
	N_2 PSD[b] (dN/dr)		N_2 PSD[b] (dV/dr)	Glatter PSD[c] (dN/dr)	
r_m (Å)	30		50	30	

	Helium Permeability			
	$T = 273$ K	$T = 308$ K	$\sqrt{308}/\sqrt{273}$	D_g^{308}/D_g^{273}
$P_{exp}\times10^3$ ($cm^2\,s^{-1}$)	8·35	8·86	1·06	1·06
$D_g\times10^3$ ($cm^2\,s^{-1}$)	19·42	20·60		
$D_g^0\times10^3$ ($cm^2\,s^{-1}$)	38·08	40·44		
κ_g	0·51	0·51		

	EMA (permeability + adsorption)[b]	*Relative surfaces (SANS + adsorption)*[d]
	$n_T \sim 8$	$C_n = 8-10$

[a]Assuming the S value from N_2 (77 K) BET.
[b]Assuming cylindrical pores.
[c]Assuming spherical pores.
[d]Based on consideration of real packing of spheres.

aforementioned results, while the pore size distribution obtained from the adsorption branch of the N_2 (77 K) isotherm can be seen in Fig. 1 (curve A).

The gas diffusion coefficient, D_g, for helium and the structure factor, κ_g, were calculated (Table 1) from the experimental values of the permeability. The value of κ_g (0·51) is higher than the expected ideal value of 1/3 for an isotropic, homoporous medium. This can be attributed to deviations from the cylindrical geometry (flattened pores) and/or the assumption of random reflection of molecules.[23] The measured values of helium permeability were constant over a wide range of pressure heads (10–900 mbar) ensuring that the membrane was crack-free and that mass transport occurred in the Knudsen regime. The Knudsen mechanism is also supported by measurements of helium permeability at different temperatures (Table 1).

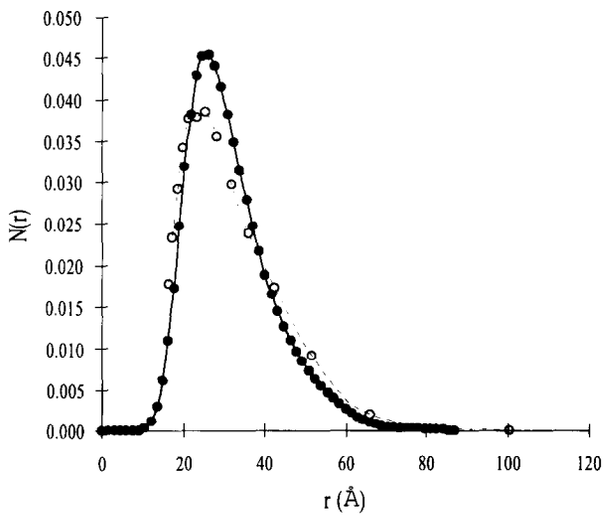

Fig. 1. Normalised pore size distributions for the Al_2O_3 membrane: (•) From SANS data, (○) From N_2 isotherm at 77 K.

Porod analysis of the SANS data for the outgassed sample gave a straight line with slope −4, which corresponds to a smooth Euclidean pore surface. The mean radius, r_m, of the medium was estimated via the Guinier approximation for long cylinders, while with the aid of the Debye–Bueche[24] relationship, the correlation length, ℓ_C, and the specific surface area, S, were calculated. These values (Table 1), as well as the pore size distribution (Fig. 1, curve B), which was obtained from the SANS data with the Glatter software, are in accordance with the ones calculated from adsorption measurements.

The transport properties of He through an alumina membrane partially blocked by water were examined by a relative permeability experiment. Figure 2 illustrates the P_R versus the amount of the adsorbed water. It becomes clear that when the amount adsorbed is between 0 and 30% of the total pore volume there is a sharp decrease in P_R while for adsorbed fractions over 30% the drop in P_R is smoother and approaches 0 before saturation

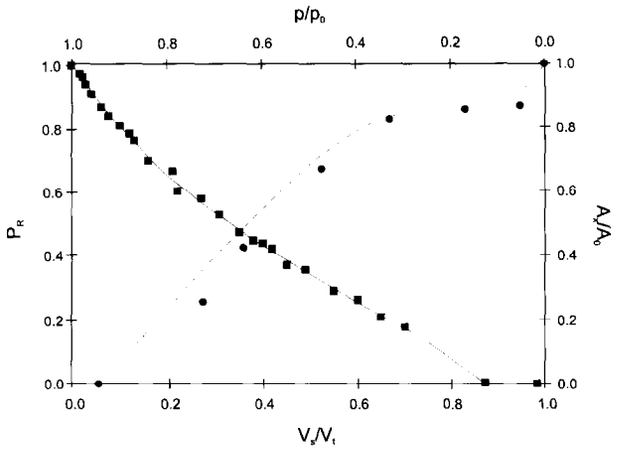

Fig. 2. Film areas and relative permeability curve for the alumina membrane.

(at $\varphi_x/\varphi_p \approx 0{\cdot}83$, a percolation threshold). By applying the Effective Medium Theory to a stochastic model the connectivity number of pores was obtained.[7] Figure 2 shows also the fitting of the model to the P_R experimental data for n_T equal to 8.

Figure 3 illustrates the scattering curves in the form of a function $Q^2I(Q)$ versus Q for an alumina membrane loaded with a H_2O/D_2O mixture at various relative pressures. During adsorption [Fig. 3(A)] the intensity of this function decreases whereas during desorption [Fig. 3(B)] it increases. This is due to the contrast matching between the solid and the adsorbate. During adsorption the pore volume which can effectively produce a scattering contrast decreases by an amount equal to the amount adsorbed, whilst during desorption the reverse course of events takes place. Therefore, integration of the $Q^2I(Q)$ function over Q may lead to an evaluation of the fraction of the amount adsorbed (φ_x). Based on the general case of the scattering theory[11] the following expression can easily be derived:

$$\frac{\tilde{Q}_x}{\tilde{Q}_0} = \left(1 - \frac{\theta_x}{\varphi_p}\right)\left(1 + \frac{\varphi_x}{\varphi_p}\right) \qquad (7)$$

where $\tilde{Q}_0$ and $\tilde{Q}_x$ are the Porod's invariants $\left(\tilde{Q} = \int Q^2 I(Q) d(Q)\right.$ at $p/p_0 = 0$ and x, respectively, and φ_x, φ_p have the same meaning as previously mentioned. By plotting φ_x/φ_0 versus p/p_0 a reconstruction of the adsorption isotherm is obtained. Figure 4 demonstrates this result, together with the adsorption isotherm of water. Taking into account the experimental uncertainty and the fact that fewer points contribute for the reconstruction than for the real isotherm, the agreement between the two curves is satisfactory.

The nature of the adsorption process can also be discussed. In relation to adsorption theory two

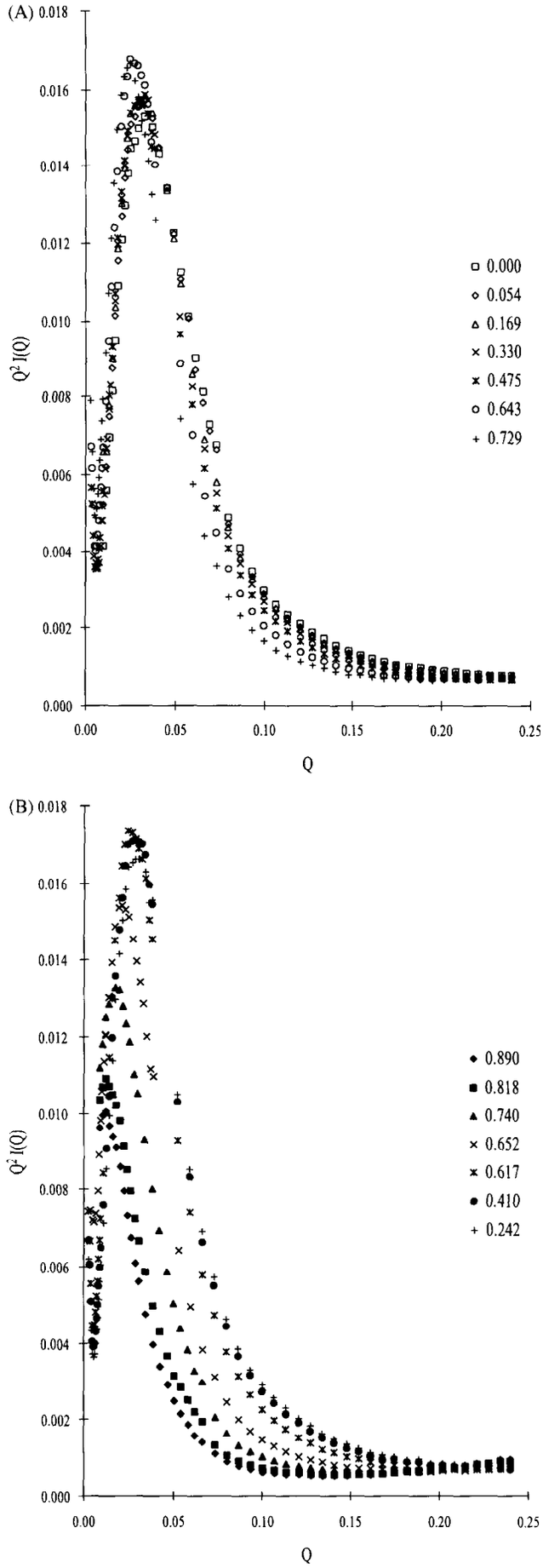

Fig. 3. Neutron scattering curves, $Q^2I(Q)$ versus Q, for the alumina membrane loaded with H_2O/D_2O at various p/p_0. (A) adsorption; (B) desorption.

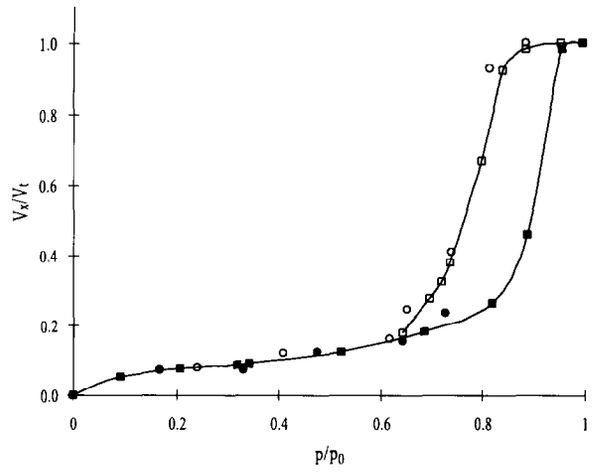

Fig. 4. The adsorption isotherm of water for an alumina membrane and the reconstruction of the adsorption isotherm from the SANS data. (•) adsorption and (○) desorption branches from SANS; (■) adsorption and (□) desorption branches volumetrically.

mechanisms may lead to a decrease in the value of $Q^2I(Q)$: (a) deposition of an adsorbed film on the pore walls and (b) condensation in an entire class of pores. It should be noted that the drop in the $Q^2I(Q)$-curve is expected to be small as a result of the first mechanism and large as a result of the second one. Returning to Fig. 3(A), at p/p^0 between 0 and 0·73 the prime mechanism is the formation of an adsorbed film on the pore walls whereas at $p/p_0 > 0{\cdot}73$ the dominant mechanism is capillary condensation. During desorption [Fig. 3(B)], at p/p_0 between saturation and 0·62 the scattering function $Q^2I(Q)$ increases relatively fast whilst between 0·62 and 0 it increases smoothly. Therefore, the dominant mechanism is evaporation with the larger pores emptying first. This conclusion is in accordance with the Kelvin equation. A careful examination of the spectra [Fig. 3(B)] shows a rather sharp decrease in the function $Q^2I(Q)$ for p/p_0 values between 0·65 and 0·62. Such relative pressures correspond to pores having a Kelvin radius of about 20 Å.

Following the above successful comparison test of the two methods (adsorption and SANS), we tried to gain information regarding the film areas for each p/p_0. This may be attained by calculating the surface area via the Porod formula [eqn (4)] and by assuming that the fraction of pores that are closed is negligible in the case of our alumina membrane. This is a quite reasonable assumption for a material produced via symmetric compaction of particles with a narrow distribution and a final porosity comparable to that of a random close packing (rcp) or a loose close packing (lcp) of spheres (0·40 versus 0·36–0·40). Since symmetric (i.e. rather homogenous) compression lead to porosities similar to those of lcp or rcp structures and, in addition, the alumina material can not flow (e.g. the way a polymer particle may do upon compression), it is rather safe to postulate that the pore network of the compressed Alumina structure should not differ in its coarse features from that of the rcp and lcp structures. Since the latter contain no closed pores we will assume that the fraction of closed pores in the compressed alumina is not significant. Figure 2 shows the result in terms of relative surface area A_x/A_0 versus p/p_0. By applying appropriate models, such as those postulated by Karnaukhov and Kiselev[18] or Wade,[19,20] the co-ordination number of the alumina membrane may be obtained. Although our experimental technique (adsorption in conjunction with SANS) was completely different from that of Wade, for similar samples the two results are comparable and a $C_n \sim 10$ was estimated for the alumina membrane. However, this method appears to systematically overestimate the true co-ordination number and an estimated C_n of 10 corresponds to an actual C_n of approximately 8.[19] A possible reason for such deviations is the difference between idealised packings characterised by point contacts of spheres and actual packings which result from compaction and include contacts of finite width. Such differences in the geometry of contacts affect the amount and geometry of the condensed phase. A co-ordination number of 8 is 'reasonable', given that the co-ordination number for random packing of spheres is in the 7 to 8 range (when counting contacts and near contacts) and also 8 is the co-ordination number for body centred cubic (bcc), a regular structure characterised by a packing density comparable to that of rcp (0·68 for bcc versus 0·637 for rcp). Hence both n_T and C_n are probably approximately equal to 8 and this is in accordance with the view that when the number of particles is equal to the number of pores between them, the values of n_T and C_n may also be equal. For example, for a simple cubic arrangement of spheres each sphere is in contact with six other spheres (i.e. $C_n = 6$), each pore communicates (shares an opening) with six surrounding pores (i.e. $n_T = 6$) and the number of spheres is equal to the number of pores.

We may conclude that by combining equilibrium and dynamic techniques it is possible to draw self-consistent conclusions that are broader than those of a single method. However, we should emphasise that the type of comparisons and conclusions possible through the application of the various methods depends on the type of material geometry as well. For instance, if there is a significant fraction of closed pores (pores inaccessible to probe molecules) or non-conducting (dead-end) ones, the estimates of the film areas will vary with the method. This is because SANS is capable of showing contributions from all types of pores, adsorption and

SANS in conjunction with adsorption open and dead end pores, while permeability data pertain to conducting pores only.

4.2 Vycor silica membrane

Adsorption in conjunction with SAS may provide a detailed information about the geometrical nature of internal surface of a porous material. Such information is of interest as in many cases the nature of the internal surface itself—in addition to the porosity level—is of critical importance for a porous material application (e.g. catalysis). Vycor® porous glass 7930 is a quite appropriate example of a commercial mesoporous material with rough surface. In this section we explore the possibility of drawing quantitative conclusions regarding the details of the hydrophilic surface and the way they change as the adsorption of water (SANS) and dibromomethane (SAXS) progresses. As in each case (SANS or SAXS) a different adsorbate is used in order to attain contrast matching it is possible to obtain different types of scattering curves, as a result of differences in the cross-sectional areas of the adsorbed molecules and also the nature of interaction between the internal surface and the adsorbate molecules.

Figure 5 shows the SANS spectra together with the mirror image of the SAXS spectra for 7930 Vycor® at various p/p_0 values. According to eqn (5), the fractal dimension D_f of the surface is related to $I(Q)$ through the expression: $I(Q) \propto Q^{D_f-6}$

According to literature views[25] about defractalization (i.e. levelling off of the surface details), when an adsorbed film of thickness t is deposited on a fractal surface, the film–vapour interface although smoother than the original substrate may also exhibit fractal features as long as the surface roughness is at a length scale much greater than t. In terms of SAS the conditions for fractal or Euclidean appearance of the film surface are $Q \cdot t \to 0$ and $Q \cdot t \to \infty$, respectively, whereas at $Q \cdot t \approx 1$ a crossover (defractalization) is observed. Table 2 summarises the fractal dimension D_f for each p/p_0. For the dry sample we have found that $D_f \approx 2{\cdot}6$. This result is in accordance with the conclusions of other investigations,[26] though reports also exist[27] that the dry surface is Euclidean. Material preparation is a possible reason for the existing controversy. This is because Vycor® is a highly hydroscopic material and incomplete drying may lead to gross geometrical changes of the surface. Actually, a careful examination of Table 2 shows that water is a much more effective agent of defractalization than dibromomethane. In particular, although dibromomethane has a much larger linear dimension than water (hence a layer of dibromomethane is much thicker than a layer of water), the defractalization point for water is at $p/p_0 = 0{\cdot}28$, whereas for dibromomethane is at $p/p_0 \approx 0{\cdot}75$. These relative pressure values imply that defractalization of water occurs near the monolayer formation ($t \approx 3$ Å while for dibromomethane this takes place after the stacking of approx. three molecular layers ($t \approx 15$ Å). The difference is clearly due to the hydroscopic nature of the Vycor® surface. As adsorption progresses the water molecules do not simply amass on the surface (as the dibromomethane molecules do), but they interact chemically with the surface. As a result the adsorbed water molecules are capable of attaching large surface silicate entities (possibly of an open fractal character, Fig. 6) to the base of the surface and also smoothen the contours of individual or small neighbouring open silicate entities. As adsorption progresses beyond the first layer, structures such as those of Fig. 6 may rearrange and

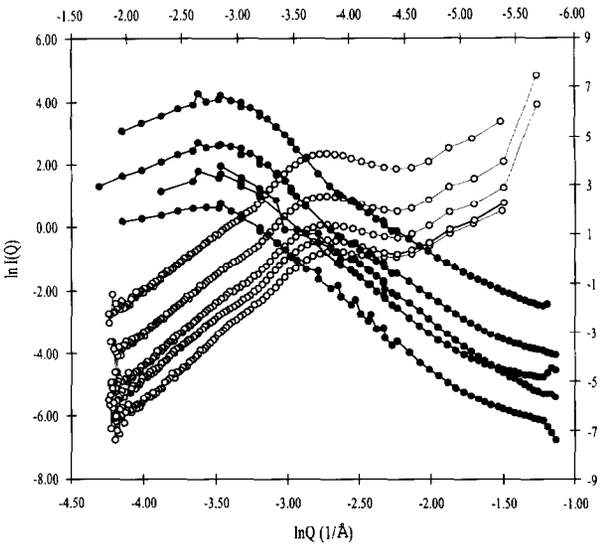

Fig. 5. Porod plots for Vycor®porous glass at various p/p_0. Filled circles denote adsorption of H_2O/D_2O in conjunction with SANS at p/p_0 (from top to bottom) 0·00, 0·28, 0·35, 0·56 and 0·64. Open circles denote adsorption of dibromomethane in conjunction with SAXS at p/p_0 (from top to bottom) 0·00, 0·34, 0·56, 0·72 and 0·76. In both cases successive curves of the spectrum have been shifted along the intensity axis by an arbitrary factor in order to avoid overlapping. Left y-axis and bottom x-axis correspond to SANS data, while right y-axis and top x-axis correspond to SAXS data.

Table 2. Fractal dimensions of Vycor®glass obtained from SANS and SAXS

p/p_0	*SANS*	*SAXS*
	D_f	D_f
0·00	2·7	2·6
0·28	2·1	nd
0·34	nd[a]	2·5
0·35	1·9	nd
0·56	1·9	2·5
0·64	1·8	nd
0·72	nd	2·4
0·76	nd	1·9

[a]nd Not determined.

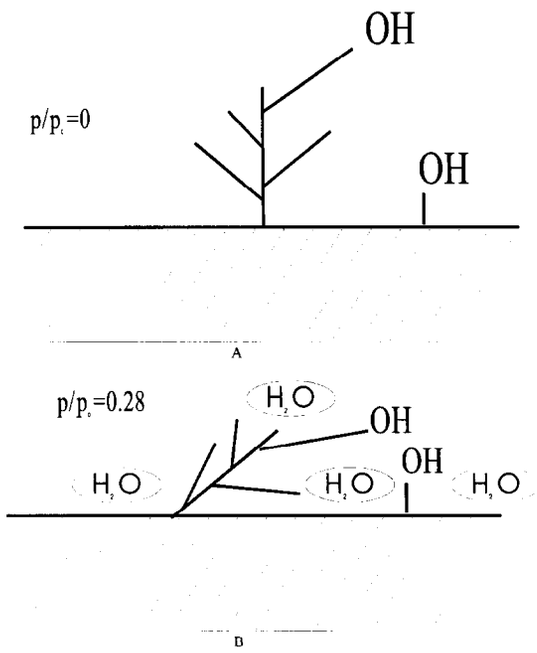

Fig. 6. The internal surface geometry of Vycor® porous glass: (A) 'dry' surface with protruding silicate entities; (B) 'Smooth' surface corresponding to a monolayer of adsorbed water.

become part of a thicker silicate hydrogel-like structure. However, the original structure pictured in Fig. 6 is not, strictly speaking, typical of a silicate hydrogel, as in the former case a small amount of water holds together relatively large entities of silicate material, while the inverse is true in the latter case.

One may note that in this discussion we have used the terms 'rough' and 'fractal' in somewhat interchangeable manner. In reality there is a physical distinction between a rough and a fractal surface, but it is very difficult to distinguish between the two via a SAS experiment. A detailed analysis of this point has been given in the pertinent literature.[28] Nevertheless, this point does not affect the essence of our conclusions regarding the interaction of the adsorbate molecules with large protruding silicate entities of the internal surface.

Although contrast matching (CM) is a technique that traditionally supplements SANS, it is also possible to use it as a supplement of SAXS (which is a much cheaper and accessible method than SANS), as we have shown in this work.

4.3 Asymmetric carbon membranes

For this material we have used a combination of three methods i.e. nitrogen adsorption, SANS and permeability. We are primarily interested in the structure of the microporous skin, as this is the membrane part capable of gas separation. Nevertheless, the substrate, in addition to its macroporosity, it also possesses microporosity which is studied as well. The macroporosity of the substrate is necessary for the fast flow of the gases through its volume and corresponds to the interparticle space of the starting material, while the microporosity is of intraparticle character and develops as the substrate material undergoes the same processing (carbonisation and activation) as the skin.

Combination of data from nitrogen adsorption (performed in the replica and the membrane bulk) and SANS (performed in replica and the composite membrane) indicates that the thin skin and the bulk (substrate) of the membrane show the following similar structural features at the $< 10^2$ Å size scale:

(a) Solid domains with a characteristic dimension of 40 Å. This conclusion is based on a Bragg peak found in the Porod plot, ln $I(Q)$ versus ln Q, of the SANS data (Fig. 7). The peak may not correspond to a pore dimension, as the shape of the nitrogen adsorption isotherms (Type I) indicate a 'purely' microporous material (i.e. the pore diameter is < 20 Å).

(b) Micropores with a diameter of 12–15 Å (based on nitrogen isotherms examined via the Dubinin–Astakhov method and a Guinier analysis of the SANS data) and a non-strongly asymmetric shape. The latter conclusion is based on the fact that the

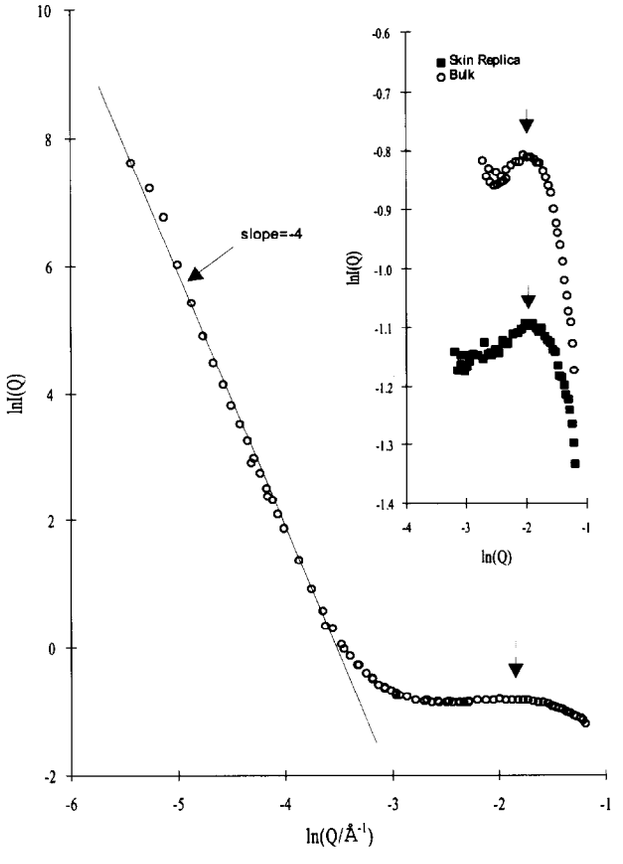

Fig. 7. Porod plot for the bulk of the carbon membrane. Inset: Porod plot for a 'replica' of the membrane skin. In both cases the arrows indicate the location of the Bragg peak.

modified-Guinier analysis [eqns (6a)–(6c)], assuming cylindrical or slit-shaped pores, leads to negative pore dimensions [Fig. 8(A)], while the corresponding analysis for spherical objects gives acceptable values [Fig. 8(B)].

(c) A microporosity level on the order of 0·30–0·38 for non-activated samples, while additional micropores of the same size are filled or blocked by disordered material and become accessible upon activation, leading to a total microporosity of approximately 0·50 and a surface area, S, on the order of $1300\,m^2\,gr^{-1}$.

Subsequently, various types of model microstructures are tested for compatibility with the above findings, with the help of a systematic classification of porous carbon microstructures which is described in detail elsewhere.[29] This compatibility test leads to the exclusion of most types of microporous carbon microstructures. For example, various arrangements of platelet-like carbon domains are not satisfactory candidates, as they can easily generate low or high levels of porosity but not intermediate ones (0·3–0·6). The survey of possible structures leads to three strong candidates, characteristics of which are pictured in Fig. 9(A)–(C).

Figure 9(A) shows a cross section of carbon domains bearing at their periphery an 'egg-case' type of pore arrangement. Figure 9(B) shows a cross section of 40 Å domains containing intradomain porosity in the form of alternating solid and void sub-domains, while the interdomain space contributes little to the total microporosity. Figure 9(C) shows a low aspect ratio cylindrical domain (with other low asymmetry domains also possible). The microstructure may then correspond to a random arrangement of such domains, while the wedge-shaped grooves allow for acceptable values of surface areas and microporosity levels of 0·4 or more. Note that the maximum width of the grooves shown (on the order of 7 Å or less) is such that the wedges can not be detected as separate objects by the SANS technique, and hence the asymmetry of those additional small micropores is not in contradiction with the (b) statement (which will still apply to the interdomain openings).

A special feature of the structure of Fig. 9(A) is that a significant fraction of the pores is

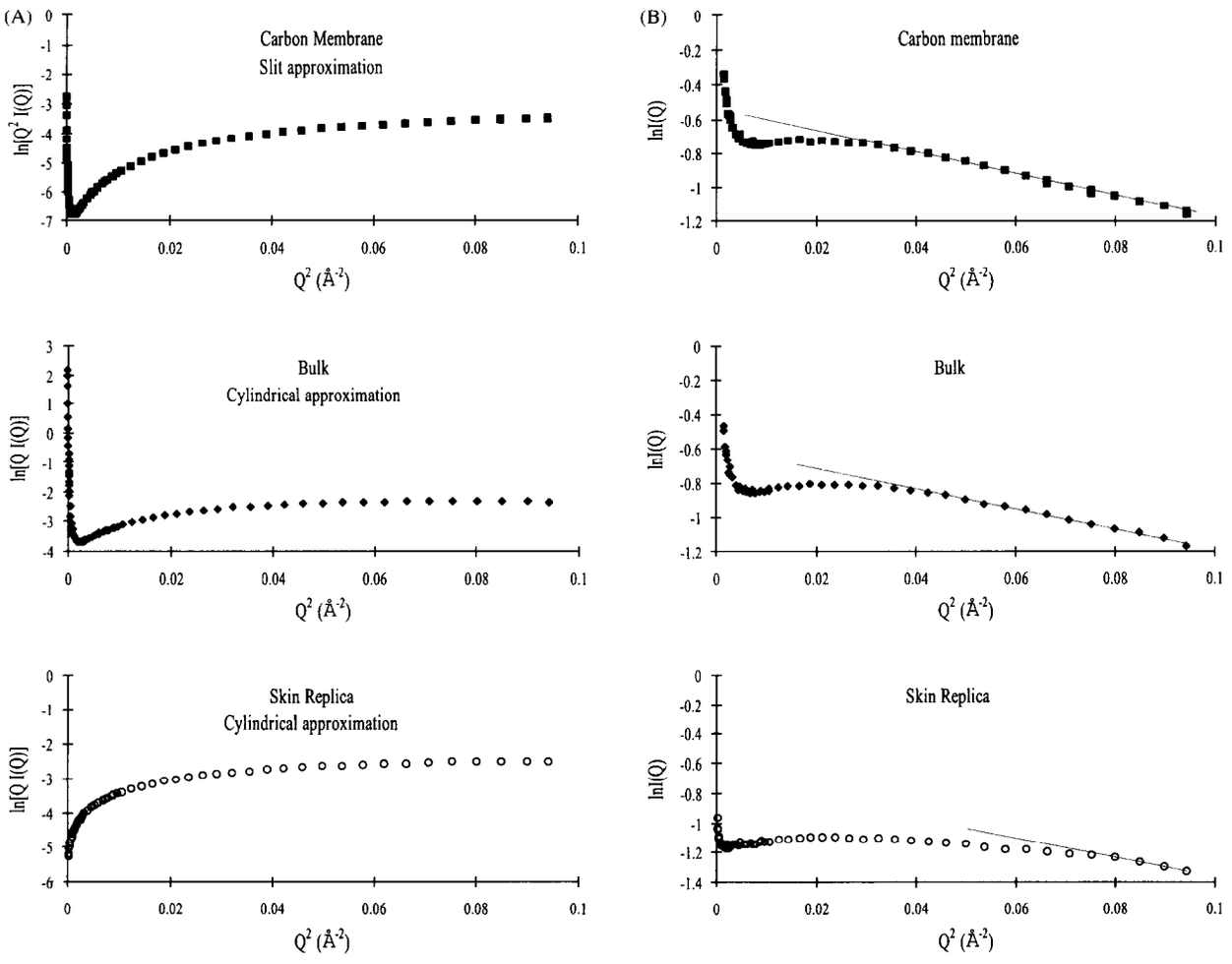

Fig. 8. Guinier and modified Guinier plots for the asymmetric carbon membrane. (A) 'Modified Guinier' plots for slit and cylindrical geometry; (B) 'Guinier' plots for the carbon membrane, the bulk of the membrane and the skin replica.

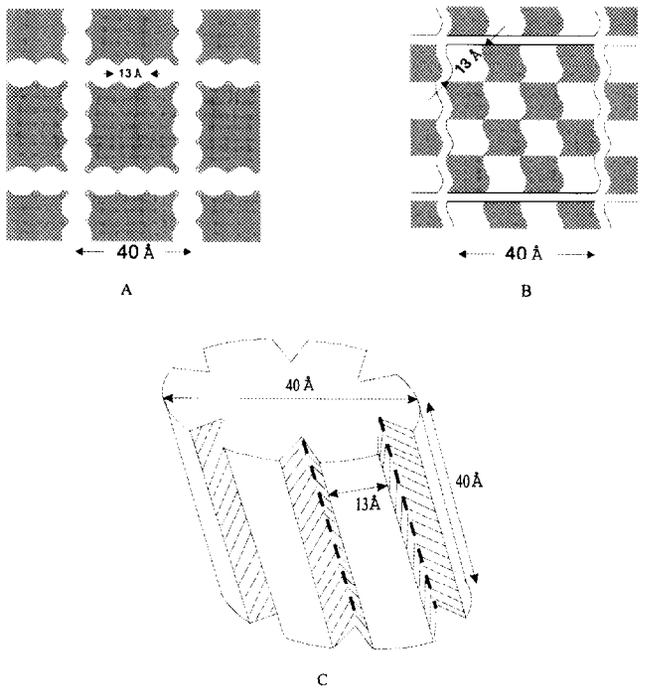

Fig. 9. Models for the carbon membrane microstructure: (A) cross-section of an arrangement of 40 Å carbon domains with peripheral microporosity; (B) cross section of an arrangement of 40 Å carbon domains with intradomain microporosity. (C) low aspect ratio cylindrical carbon domain with wedge-shaped surface details. A microstructure model corresponds to a random packing of such domains.

characterised by 2-D connectivity. From integral permeability experiments with helium, the structural factor κ_g [eqn (2)] for an asymmetric membrane is estimated to be in the range of 8×10^{-5}, a value which appears to favour the microstructure of Fig. 9(A). This is because a very low value of the structure factor for a carbon membrane having a skin with a microporosity of approximately 0·38, may signify an unusually long (tortuous) path necessary for permeability and therefore, the porous structure should be in the vicinity of its percolation threshold. As the percolation threshold should be near 0·15 for a three-dimensional pore arrangement and near 0·50 for a two-dimensional arrangement, a percolation threshold in the vicinity of 0·38 indicates that the pore arrangement has a partial two-dimensional character. Nevertheless, an alternative explanation for the observed very low structure factor is the presence of constrictions. The models of both Fig. 9(A) and (B) are capable of generating strong constriction effects.

Finally, in Fig. 10 we see the results of differential permeability of the carbon membrane for slightly supercritical ($T = 35$°C) carbon dioxide.[8] The sharp maximum is observed at a pressure of 35 bars and can be attributed to the special ordering of the CO_2 molecules inside the micropores. Following Nicholson *et al.*[30] the flux in the x-direction is given by the expression:

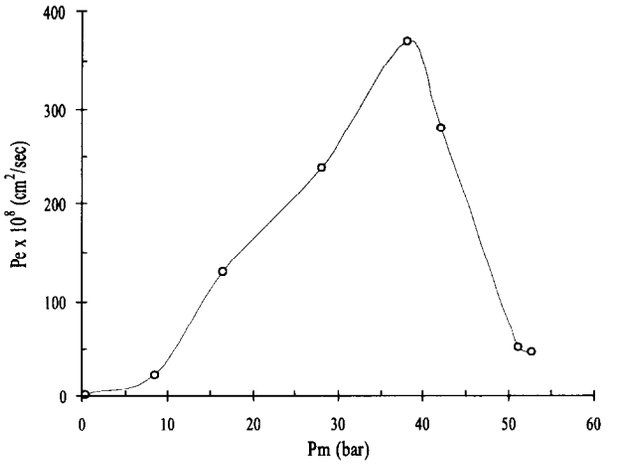

Fig. 10. Differential CO_2 permeability curve at 308 K for the composite carbon membrane.

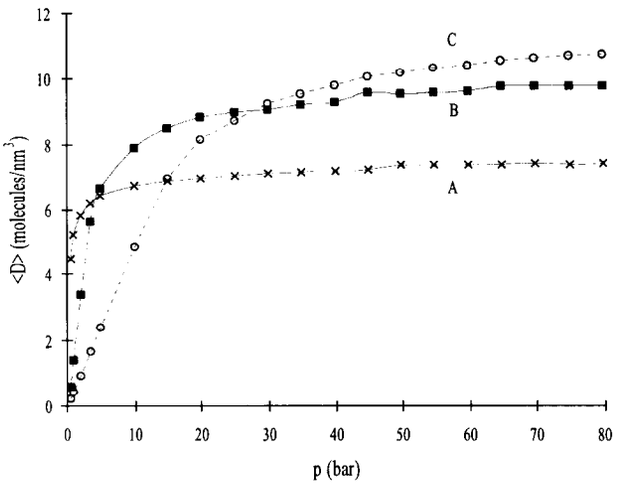

Fig. 11. Mean density of CO_2 at 308 K inside micropores versus pressure (Monte Carlo simulation): (A) pore width = 7·5 Å; (B) pore width = 10·5 Å; (C) pore width = 15·5 Å.

$$J = J_D + J_V = -\frac{cD}{kT}\left(\frac{\partial\mu}{\partial x}\right) - \frac{cB_0}{\eta}\left(\frac{\partial p}{\partial x}\right) \qquad (8)$$

where J_D is diffusive flux, driven by the chemical potential, $\partial\mu/\partial x$, J_V is viscous flux, driven by the pressure gradient, $\partial p/\partial x$, c is molecular concentration inside the pore space, D is diffusion coefficient, k is the Boltzmann constant, T is absolute temperature, B_0 is geometrical term, and η is the viscosity coefficient.

Non Equilibrium Molecular Dynamics (NEMD) studies revealed that for certain micropores viscous contribution is activated above a critical density (and therefore pressure) of the fluid inside the pores. At lower pressures the diffusive flux is predominant, while in higher pressures the viscosity coefficient increases rapidly. This situation will eventually lead to a maximum in the permeability, as predicted for the permeability of supercritical CH_4 through a 0·95 nm width slit-shaped carbon micropore.[30]

On the other hand a Monte Carlo (MC) simulation[9] for carbon dioxide in supercritical conditions is currently used to estimate the density profile (and, as a result, the mean density) of the fluid inside carbon slits at various pressures (Fig. 11). We expect that ultimately a combination of such NEMD and MC simulations, will permit the determination of pore width from the high pressure differential permeability data.

5 Conclusions

The combination of structural characterisation methods (equilibrium or dynamic ones) leads to an enhanced spectrum of pore geometry information for three important ceramic membrane materials.

For the mesoporous alumina membrane we combined adsorption, permeability, SANS, relative permeability and adsorption in conjunction with SANS, reconstructed the adsorption isotherm from SANS data, calculated the coordination number of the solid entities from the adsorbed film areas and also estimated the pore connectivity number from the relative permeability data. The connectivity number and coordination number were estimated as approximately equal to 8, a value which is compatible with the type of structure expected for this material.

For the mesoporous Vycor® silica membrane we combined adsorption with SAXS and SANS and monitored in detail the process of defractalization for the internal surface. It was concluded that water is a very efficient defractalization agent due to its ability to attach large silicate entities to the base of the internal surface and also smoothen the contours of individual silicate entities.

For an asymmetric carbon membrane we combined information from adsorption, SANS, integral and differential permeability. The selective layer and the bulk of the membrane were found to share various structural features at the $< 10^2$ Å size scale. According to the micro-structural model most compatible with our experimental findings, the building block of the microstructure is a low aspect ratio carbon domain with a characteristic dimension of 40 Å. The micropores of 13 Å diameter are probably located at the periphery of the domains in an 'egg-case' type of arrangement.

Acknowledgements

The Human Capital Mobility program of the European Commission is gratefully acknowledged.

References

1. Brunauer, S., Deming, L. S., Deming, W. S. and Teller, E., *J. Amer. Chem. Soc.*, 1940, **62**, 1723.
2. Roberts, B. F., *J. Colloid Interface Sci.*, 1967, **23**, 266.
3. Dubinin, M. M., *Russ. J Phys. Chem.*, 1965, **39**, 697.
4. Ash, R., Baker, R. W. and Barrer, R. M., *Proc. Roy. Soc. (London) A*, 1967, **299**, 434.
5. Ash, R., Barrer, R. M. and Sharma, R. J., *J. Membr. Sci.*, 1976, **1**, 79.
6. Kanellopoulos, N. K., and Petropoulos, J. H., *J. Chem. Soc., Faraday Trans. I*, 1983, **79**, 517.
7. Steriotis, T. A., Katsaros, F. K., Stubos, A. K., Mitropoulos, A. Ch. and Kanellopoulos, N. K., *Measurements Science and Technology*, 1997, **8**, 168–173.
8. Katsaros, F. K., Steriotis, T. A., Stubos, A. K., Mitropoulos, A., Kanellopoulos, N. K. and Tennison, S., *Microporous Materials*, 1997, **8**, 171–176.
9. Samios, S., Stubos, A. and Kanellopoulos, N., A Monte Carlo simulation for the behavior of slightly supercritical carbon dioxide inside carbon micropores, in preparation.
10. Debye, P. J. W., Anderson, Jr, H. R. and Brumberger, H., *J. Appl. Phys.*, 1957, **28**, 679.
11. Guinier, A. and Fournet, G., *Small-angle Scattering of X-rays*, Wiley, New York, 1955.
12. Bale, H. D. and Schmidt, P. W., *Phys. Rev. Lett.*, 1984, **53**, 596.
13. Hall, P. G. and Williams, R. T., *J Colloid Int. Sci.*, 1985, **104**(1), 151.
14. Glatter, O., *J Appl. Cryst.*, 1984, **17**, 435.
15. Kikkinides, E. S., Tzevelekos, K. P., Stubos, A. K., Kainourgiakis, M. E. and Kanellopoulos, N. K., *Chem. Eng. Sci.*, 1997, **52**(16), 2837–2844.
16. Steriotis, Th., Katsaros, F. K., Mitropoulos, A., Stubos, A. K. and Kanellopoulos, N. K., *J. of Porous Materials*, 1995, **2**, 281.
17. Mitropoulos A. Ch., Haynes, J. M., Richardson, R. M. and Kanellopoulos, N. K., *Phys. Rev. B*, 1995, **52**, 10035.
18. Kamaukhov, A. P. and Kiselev, A. V., *Russ. J. Phys. Chem.*, 1960, **34**, 1019.
19. Wade, W. H., *J. Phys. Chem.*, 1964, **68**, 1029.
20. Wade, W. H., *J. Phys. Chem.*, 1965, **69**, 1395.
21. Magoulianiti, E., Beltsios, K., Davazoglou, D., Romanos, G., and Kanellopoulos, N., Chemical vapor deposition of SnO2 films within the pores of vycor substrates for the control of their porosity. Proceedings of the International Symposium on International Chemical Vapor Deposition: CVD-XIV and EUROCVD I I Symposium, Paris, (1997).
22. Steriotis, T. A., Katsaros, F., Stubos, A. K., Mitropoulos A. Ch., Galiatsatou, P. and Kanellopoulos, N. K., *Review of Scientific Instruments*, 1996, **67**(7), 2545–2548.
23. Barrer, R. M., The solid–gas interface, Vol. 2, ed. E. A. Flood, Marcel Dekker, New York, 1967.
24. Debye, P. J. W. and Bueche, A. M., *J. Appl. Phys.*, 1949, **20**, 518.
25. Cheng, E., Cole, M. W. and Pfeifer, P., *Phys. Rev. B*, 1989, **39**, 12962.
26. Levitz, P., Ehret, G., Simha, S. K. and Drake, J. M., *J. Chem. Phys.*, 1991, **95**, 6151.
27. Schaefer, D. W., Bunker, B. C. and Wilcoxon, J. P., *Phys. Rev. Lett.*, 1987, **58**, 284.
28. Po-zen, Wong, *Phys. Rev. B*, 1985, **32**, 7417.
29. Steriotis, Th., Beltsios, K., Mitropoulos, A. Ch., Kanellopoulos, N., Tennison, S., Wiedenman, A. and Keiderling, U., *J. Appl. Polymer Sci.*, 1997, **64**, 2323–2346.
30. Nicholson D., Cracknell, R., *Langmuir*, 1996, **12**(16), 4050.